JOHN C. MURPHY, LEONARD C. AAMODT, FRANK G. SATKIEWICZ,
R. BEN GIVENS, and P. RONALD ZARRIELLO

MATERIALS AND MICROSTRUCTURE

A knowledge of the microstructure of electronic materials and devices as well as structural materials is a key factor in understanding their properties. Thermal wave imaging is a relatively new technique that provides images that display microstructural features; it also allows local material properties to be measured. The technique has been used to locate localized defects (such as subsurface cracks and voids) in metals and ceramics and to study grain structure in metals. Contrast mechanisms in imaging are discussed, and various thermal wave techniques are described and compared.

INTRODUCTION

New materials with special properties have played a prominent role in the history of human civilization. Epochs entitled the Stone, Iron, and Steel Ages (and perhaps now the Silicon Age) give a sense of the impact these developments have had on human affairs. What is sometimes overlooked is that the elemental composition of these materials defines their properties only to a limited extent. Cast iron and steel, for example, can have the same elemental composition yet have significantly different properties because of the special grain structure present in steel that arises from the processes of heat treatment and metalworking used in its formation. Microstructure can determine macroscopic properties.

Fiber-matrix composites and crystalline ceramics provide another example. Here two or more distinct materials are brought together in a controlled structure to produce a final product with properties measurably different from those of either of the starting constituents. Again, microstructure determines macroscopic properties at the price of complex spatial variations in sample properties across the specimen. Conversely, microstructural failure of the fiber-matrix bond in the composite or microcracking in the ceramic implies failure of the larger structure.

Semiconductors provide a final example. Here, device performance is jointly determined by specimen properties; intentional structure is provided by circuit architecture, and unintentional structure is represented by processing defects, dislocations, grain boundaries, and other flaws in the base material. As the scale of electronics continues to shrink, the role of microstructure will continue to grow. For some structured materials now under development, ordering occurs at the atomic or molecular level, and the question of microstructural control becomes more important.
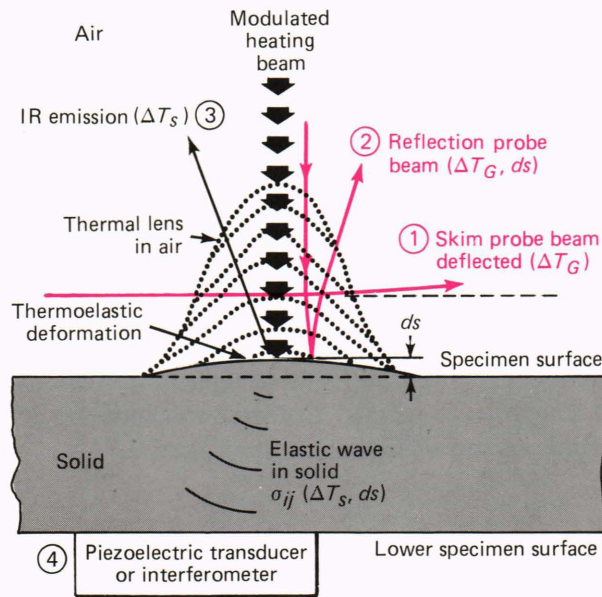
THERMAL WAVE IMAGING

Our everyday experience with the diffusive nature of heat suggests that temperature is an unlikely tool for studying microstructure; nevertheless, temperature patterns produced by modulated heating provide an excellent way to study the local properties of many solids and to study specimen microstructure as well.

Thermal wave imaging refers to a family of methods that uses time-varying changes in sample temperature to study the local properties of solids.[1-3] The modulated sample temperature is produced by a modulated excitation source that is scanned over the specimen surface. An image, obtained by monitoring some temperature-dependent property during the scan, provides information about the optical, electronic, structural, and thermal properties of the specimen. In addition, when particle beams such as electron and ion beams are used for excitation, the image contains information about the nature of the beam-specimen interaction, including possible nonthermal interactions.

Figure 1 illustrates some basic features of thermal wave imaging. A time-varying energy beam incident on the sample is fractionally absorbed and converted to heat with a consequent rise in specimen temperature. The modulated temperature changes a number of specimen properties, and several of these can be used to determine both the volume and surface temperature. Members of the family of thermal wave imaging methods are classified by the physical property used for detection and by the source used for excitation. Several detection methods are schematically represented in Fig. 1; their characteristics are summarized in Table 1. Specific features of the methods illustrated will be discussed later. For now, note that the images obtained on a given sample using different detection methods can differ radically even though they are initiated by the same temperature change. The reason lies in the role of the thermal parameter being detected and its effect on image contrast. The issue of image contrast is basic to the use of thermal wave imaging methods as quantitative tools for materials characterization and nondestructive evaluation of materials. The quantitative interpretation of image data is currently one of the important research topics in the field.

Figure 1—Composite sketch summarizing several thermal wave imaging methods: (1) optical beam deflection, (2) reflective optical beam deflection, (3) infrared radiometric, (4) thermoelastic (transducer or interferometric). (T_G is the gas temperature.)

THEORETICAL BACKGROUND

For an elastic solid illuminated by a modulated excitation source, the temperature and elastic displacement are determined by the two coupled thermoelastic equations,[4]

$$\nabla^2 T - \alpha^{-1} \, \partial T/\partial t = -H/\kappa + (T\, \beta_t B/\kappa)\, \nabla \cdot \partial \mathbf{u}/\partial t \tag{1}$$

$$\nabla^2 \mathbf{u} + (1 + \lambda/\mu)\, \nabla\, (\nabla \cdot \mathbf{u}) - (\rho/\mu)\, \partial^2 \mathbf{u}/\partial t^2$$
$$= (\beta_t B/\mu)\, \nabla T, \tag{2}$$

where T is the temperature, $\mathbf{u}$ is the elastic displacement vector, κ is the thermal conductivity, α is the thermal diffusivity, β_t is the volume thermal-expansion coefficient, λ and μ are the Lamé constants, ρ is the density, and B is the bulk modulus. H is the thermal source term, which in general varies throughout the volume of the specimen. The specific form that H assumes depends on the source and the nature of the beam-specimen interaction. (No mechanical source term is assumed.)

Equation 1 is the heat equation that governs heat flow within the sample. The final term on the right-hand side of the equation represents the heat produced by elastic motion of the specimen; in many cases, it can be neglected. With that term omitted, the equations are partly decoupled, and the specimen temperature can be found by solving Eq. 1 alone without knowledge of the elastic displacement field. Equation 2, on the other hand, is the thermoelastic equation; therefore, the thermal expansion term on the right-hand side is the only source term present and cannot be omitted. Based on this analysis, the dynamic thermal imaging methods represented in Fig. 1 can be divided into (a) purely thermal imaging methods based exclusively on the solution to Eq. 1 and (b) thermoelastic methods using attached transducer detection or interferometric detection based on Eq. 2. Solution of Eq. 2 assumes that solutions of Eq. 1 are known.

"THERMAL" THERMAL IMAGING

A complete analysis of imaging using focused laser or particle beams requires the solution of Eqs. 1 and 2. For purely thermal imaging, however, the basic physical principles underlying the relationship between modulated temperature, heat flow, and materials properties can be visualized using a one-dimensional model. In one dimension, Eq. 1 becomes

Table 1—Characteristics of thermal wave imaging detection methods.

| Method | Temperature monitored | Mechanism | | Detection | | Effect measured |
		Major mechanism	Diffusion dependent	Type of localization	Scalar or vector	
Photoacoustic	Surface	Thermal	Yes	Nonlocalized	Scalar	Gas pressure
Optical beam deflection	Surface	Thermal	Yes	Line	Vector	Refractive index
Reflective optical beam deflection	Surface	Thermal and mechanical	Yes	Point	Vector	Local surface distortion
Piezoelectric transducer	Bulk	Thermo-elastic	No	Point	Scalar	Stress waves
Infrared radiation	Surface	Thermal	Yes	Point	Scalar	Optical emission
Interferometric	Bulk	Thermo-elastic	No	Point	Scalar	Surface motion

$$\partial^2 T / \partial z^2 - \alpha^{-1} \partial T / \partial t = -H(z,t)/\kappa \, , \qquad (3)$$

where $H(z,t) = H_0 \exp(-\beta z) \exp(j\omega t)$. This choice of H applies to the specific case of optical or laser illumination and for specimens with optical absorption followed by a rapid conversion to heat. Other forms of H are appropriate for ion or electron beams and for samples such as semiconductors with long carrier lifetimes. When energy storage and migration occur outside the thermal system, the analysis must also be modified to include these effects.[5,6]

Figure 2 shows a sample specimen mounted on a transparent substrate, with its top face in contact with air. In each region, α is constant. Under these conditions, the surface temperature is

$$T(z=0) = T_s = \frac{\delta(\beta\delta)}{\kappa}$$

$$\times \left[\frac{1}{1 + \beta\delta} + \frac{2\Gamma \exp(-2d/\delta)}{1 + \Gamma \exp(-2d/\delta)} \frac{\beta\delta}{1 - \beta^2\delta^2} \right], \quad (4)$$

where $\delta = \sqrt{\alpha/j\omega}$ is the complex thermal diffusion length and

$$\Gamma = \left(\frac{\delta}{\kappa} - \frac{\delta_s}{\kappa_s} \right) \Big/ \left(\frac{\delta}{\kappa} + \frac{\delta_s}{\kappa_s} \right)$$

describes the thermal mismatch with the substrate at the interface (s indicates substrate). Note that the relative optical absorption spectra, $\beta(\lambda)$, can be found by measuring T_s when $d/\delta > 1$ and $\beta\delta \ll 1$. In this case,

$$T_s = (\delta^2/\kappa) \, \beta(\bar{\lambda}) \, . \qquad (5)$$

By sweeping through a range of excitation beam wavelengths, $\bar{\lambda}$, an optical spectrum can be obtained. Since Eq. 5 is valid even for a sample with no light transmission, the optical spectra of opaque materials can be obtained as well as the spectra of other materials such as gels, pastes, and highly scattering materials that can-
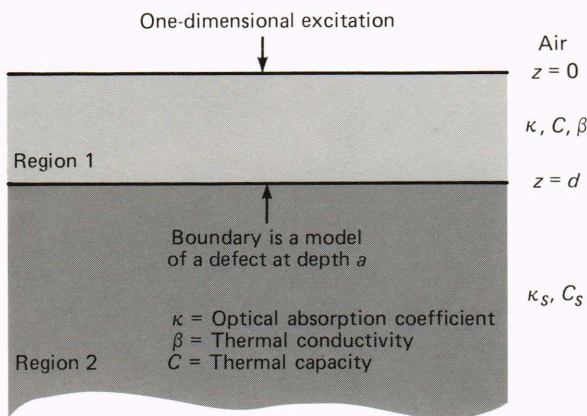
not be studied using conventional optical techniques. This is the basis of photoacoustic spectroscopy.

When $\beta\delta > 1$ and $d/\delta > 1$, $T_s = \delta/\kappa$, and it is independent of β. In this "photoacoustic saturation" regime, T_s depends principally on the thermal properties of the sample, C and κ. It also depends on microstructural features such as cracks, voids, and grain boundaries, which inhibit heat flow. To illustrate this, assume that a void exists at $z = d$. For a void, $\kappa_s C_s \approx 0$ and $\Gamma = -1$. If the sample is also opaque, ($\beta d \gg 1$) and

$$T(z=0) = T_s = \frac{\delta}{\kappa} \left[1 + \frac{2 \exp(-2d/\delta)}{1 - \exp(-2d/\delta)} \right]. \quad (6)$$

As is apparent in Eq. 6, the presence of the void at $z = d$ affects ($T(z=0)$ only when $d/\delta < 1$. As δ changes with the modulation frequency, ω, it is possible to vary δ/d above and below 1 and hence to change T_s based on the location of the lower boundary layer. This is an example of the depth profiling ability of thermal wave imaging. Experimental examples of depth sensing are presented later. Note that lateral thermal boundaries associated with surface breaking cracks and grain boundaries can show effects similar to those discussed here for depth profiling when a focused exciting beam is used.[7] This will be illustrated later for grain boundary contrast. Also, under the same conditions,

$$T(z) = \frac{\delta}{\kappa} (\beta\delta) \left\{ \frac{e^{-z/\delta}}{1 + (\beta\delta)^2} + \frac{e^{-\beta z} - e^{-z/\delta}}{1 - (\beta\delta)^2} \right.$$

$$\left. + \frac{\Gamma e^{-2d/\delta}}{1 + \Gamma e^{-2d/\delta}} \left[\frac{2\beta\delta \, e^{-z/\delta}}{1 - (\beta\delta)^2} + \frac{e^{z/\delta} - e^{-z/\delta}}{1 - \beta\delta} \right] \right\} \quad (7)$$

if $\beta d \gg 1$. This result applies to thermoelastic imaging experiments where bulk temperature is important.

THERMOELASTIC IMAGING FUNDAMENTALS

Two thermal wave imaging methods designated in Fig. 1 use piezoelectric transducers or optical interferometers to detect specimen strain produced by modulated thermal expansion. This process is described in principle by the solution of Eq. 2 for the displacement $\mathbf{u}(r,t)$, assuming that T is known from Eq. 1 and that appropriate elastic boundary conditions are also known. This problem has not been solved for the general case of continuous wave excitation. However, some analysis is available in special cases.

Certain features of the problem are immediately evident. First, the elastic displacement, $\mathbf{u}(r,t)$, depends on the elastic properties and structure of the specimen as well as on thermal properties. The relative importance of thermal and elastic contrast mechanisms in the image formation process is an important current topic for study. Second, elastic waves are generated throughout the sample wherever temperature gradients exist. These waves propagate to the surface with little differential phase delay, since the wavelength of sound waves is

One-dimensional excitation

Air
z = 0

κ, C, β

Region 1

z = d

Boundary is a model of a defect at depth *a*

κ_s, C_s

κ = Optical absorption coefficient
β = Thermal conductivity
C = Thermal capacity

Region 2

Figure 2—Cross-sectional view of layered sample.

longer than the sample size for the modulation frequencies used for thermal wave imaging. Hence, the source of the elastic effects measured by the piezoelectric transducer or interferometric detector is that portion of the sample volume where the modulated temperature is large.

Thermoelastic imaging can also detect a buried layer in an opaque specimen. Both $T(z)$ and $T(z=0)$ depend on the layer depth, d, in Fig. 2 by means of Eqs. 4 and 7. The bulk temperature is more sensitive to the presence of the buried subsurface layer than the more distant surface temperature, T_s; hence we should expect thermoelastic imaging to show greater sensitivity to subsurface objects then purely thermal imaging. This expectation has been confirmed.

After generation, the acoustic wave propagates through the sample and is reflected by elastic boundaries and interfaces. This elastic microstructure contributes to the image contrast in addition to the thermal microstructure. In fact, thermoelastic imaging has been compared in some of its features to high-frequency (> 400 kilohertz) acoustic microscopy where only elastic contrast is present.[8] The detail revealed in the images makes this a potentially powerful method if a detailed analysis can be developed to obtain quantitative data about specimen properties.

OVERVIEW OF IMAGING METHODS

Table 1 summarizes some of the detection methods used for thermal wave imaging. The three major thermal methods—photoacoustic, optical beam deflection, and infrared imaging—measure different specimen parameters but ultimately monitor T_s, the specimen surface temperature. The types of localization possible with the three methods differ. The photoacoustic technique measures the temperature integrated over the entire specimen surface, with localization being entirely dependent on the use of a localized excitation source such as a fo-cused laser or particle beam. The optical beam deflection technique measures components of the temperature field along the path of the probe rays, a process discussed in more detail in the following section. The infrared technique is in principle a point technique, while in practice it measures infrared emission over a small region of the sample. All three have approximately equal sensitivity in that they can detect modulated temperature changes of 10^{-3} °C or less.

Figure 3 shows the optical beam deflection process in greater detail and the temperature pattern produced in the gas layer in thermal contact with the specimen. The probe laser beam passes through the temperature region somewhat off the center of the exciting beam and is deflected by the time-modulated thermal lens produced by the thermally induced index of refraction gradient in the air above the sample surface. The beam deflection can be decomposed into components normal or transverse to the sample surface. The normal component is maximum when the probe and exciting beams intersect and has been shown to be proportional to the sample surface temperature.[9] The transverse component, on the other hand, is null when the probe and excitation beams intersect, reversing sign at that point. This component has been shown to be proportional to the specimen temperature gradient perpendicular to the probe ray in the plane of the sample. The transverse optical beam deflection signal is particularly useful in studying sample heterogeneity. For a radially symmetric source and a homogeneous sample, the surface temperature is symmetric, and the transverse signal is null when the probe and excitation beams intersect. However, a thermal boundary in the plane of the specimen breaks the thermal symmetry and causes the transverse deflection near the boundary to appear as a signal against a null background.

The variant of the optical beam deflection process labeled 2 in Fig. 1 (the reflective optical beam deflection)

Figure 3—Schematic of the optical beam deflection imaging method showing the two deflection components mentioned in the text.
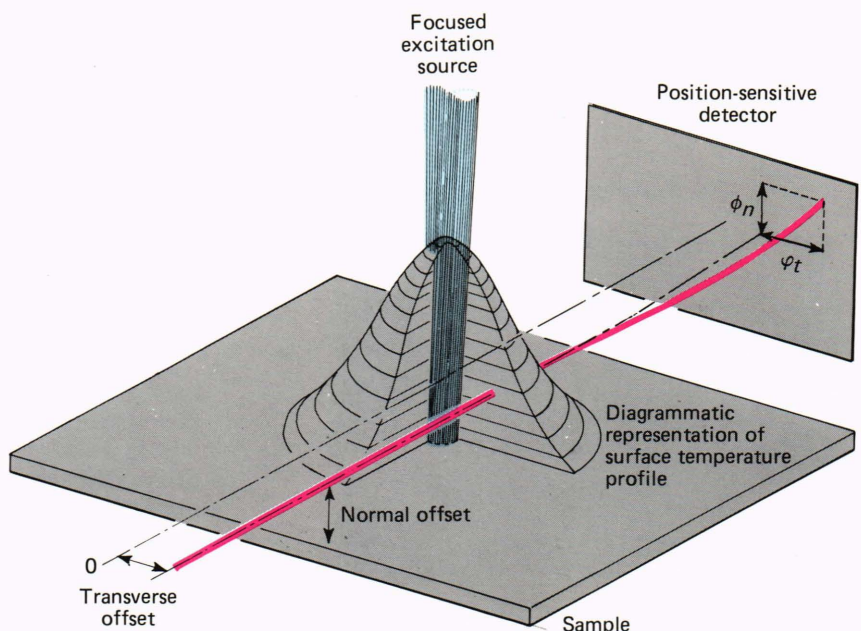
has elements of both thermal and thermoelastic imaging. In this method, the probe beam strikes the sample and is reflected. The ray path of the reflected ray is deviated by the thermal lens as in optical beam deflection imaging and also by the thermoelastically induced curvature of the surface.

The thermoelastic imaging methods measure specimen elastic response at points away from the point where heating occurs. The delay time for elastic wave propagation from source to detector is much faster than thermal diffusion times. Hence, the range of modulation frequencies that can be used in thermoelastic experiments ($20 < f < 10^6$ hertz) is much greater than in optical beam deflection and other thermal imaging ($20 < f < 10^4$ hertz). The image formation time for thermoelastic imaging is shorter than purely thermal imaging; in addition, some improvement in resolution is possible because of the smaller values of δ and the resultant reduced lateral thermal spreading.

EXPERIMENTAL THERMAL IMAGING

Figure 4 shows a system used to obtain simultaneous optical beam deflection and piezoelectric transducer images. The acousto-optic modulator allows amplitude and position modulation of the beam from the argon laser. For the ordinary case of harmonic modulation, the magnitude and phase of both detected signals are available from the lock-in amplifier for imaging. When thermal effects are important, the phase signal offers the advantage that incidental changes in specimen reflectivity do not contribute to the measured signal and that phase delays associated with thermal diffusion can be measured directly. Sample motion using a computer-controlled *x-y* stage allows scanning of the exciting beam relative to the sample. The probe beam retains a fixed position relative to the exciting beam in this configuration. The experiment was designed to explore differences in image contrast between the two methods. Since optical beam deflection detection is thermal while piezoelectric transducer detection is thermoelastic, the images should show characteristic differences if elastic contrast effects are important.

Figure 5 shows optical beam deflection and piezoelectric transducer magnitude images of a sample of the aluminum alloy 2024-T.[10] The specimen was fabricated to study the effect of lateral thermal impedance on image contrast. Two aluminum sections were cut, lapped, polished, and then joined along their polished faces by clamping. The top and bottom faces that contained the line of joining were also polished so that (except at the specimen edges) the joint was not seen in a standard normal incidence image taken with a scanning electron microscope. The width of the joined region estimated from scanning electron microscope images at the sample edges was approximately 2 micrometers.

Most features seen in the normal optical beam deflection image (Fig. 5c) and the piezoelectric transducer image (Fig. 5d) are metallic inclusions formed of elements present in the alloy. The close similarity of the two images suggests that elastic contrast is unimportant for this experimental condition. The inclusions are less evident in the transverse amplitude image (Fig. 5a) and absent in the transverse phase image (Fig. 5b). The images suggest that the inclusions are thermally coupled to the matrix, since little phase delay occurs. Other aluminum alloy specimens, especially those where fatigue processes have occurred, show large phase contrast at inclusions, presumably because of inclusion-matrix disbonding and poor thermal contact. A second conclusion is that the interface is made visible in the transverse deflection images because it inhibits thermal flow and influences the component of the temperature gradient perpendicular to the boundary. The scalar temperature images show no evidence of a boundary.

In a related experiment, cracks produced in notched tensile specimens of a naval aluminum alloy by tensile loading were studied. In regions where incomplete closure of the crack occurred, both normal and transverse components were seen; but where closure occurred, only the transverse component showed the presence of the
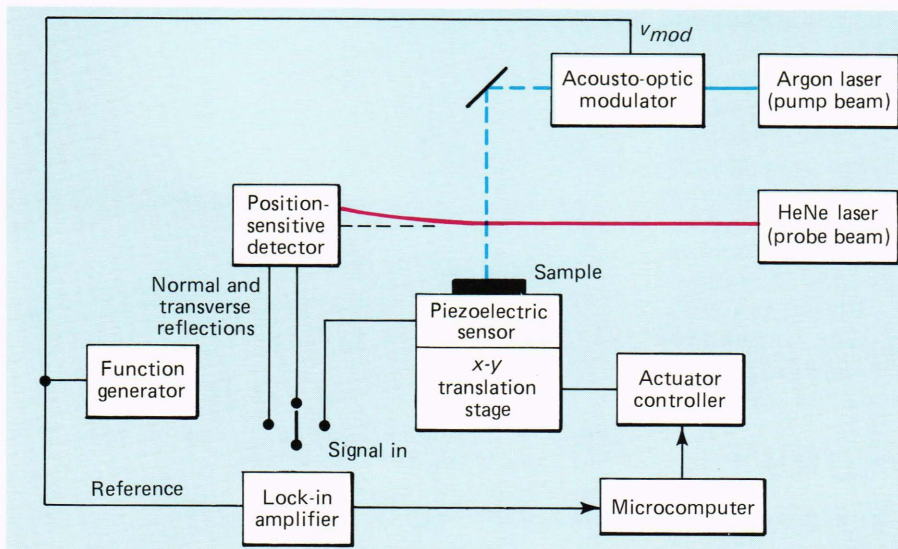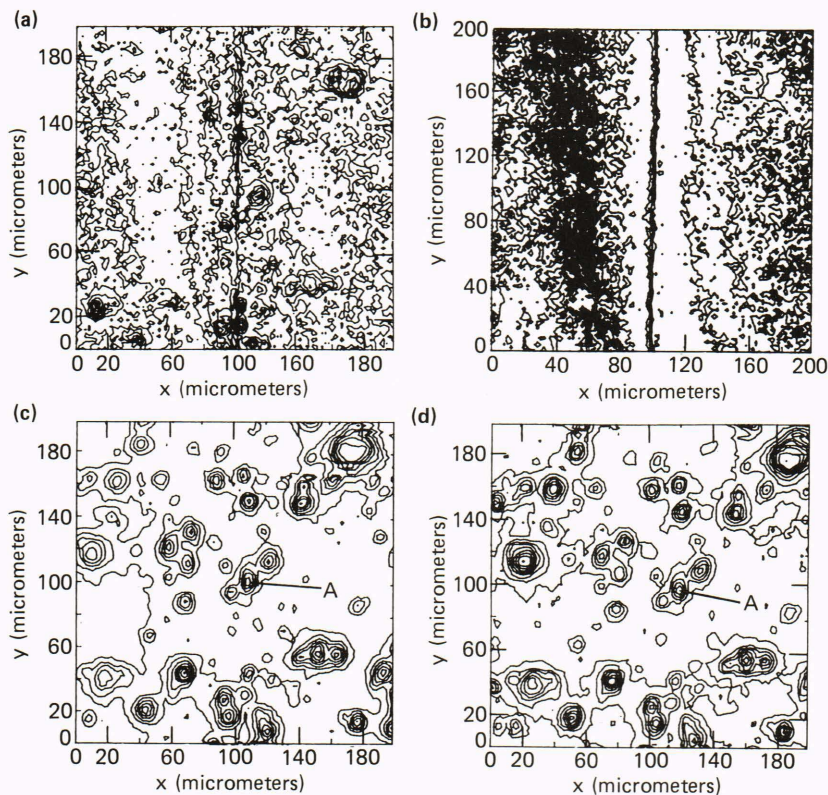

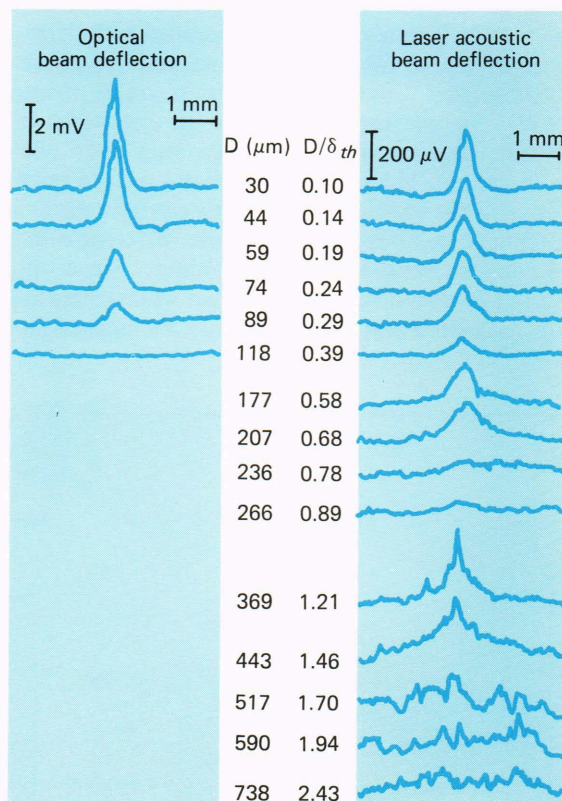**Figure 4**—Block diagram of laser source optical beam deflection and acoustic imaging system.

Figure 5—Contour images of a fabricated crack sample: (a) transverse magnitude, (b) transverse phase, (c) normal magnitude, and (d) piezoelectric transducer magnitude. Inclusions are seen in (a), (c), and (d) and the crack only in (a) and (b), as discussed in the text.

thermal boundary. This is consistent with the results obtained on the fabricated sample. In addition, some evidence of a plastic zone ahead of the crack tip was seen. This region is predicted by the theory of fracture mechanics; it is important for studies of the mechanisms of crack advance and, hence, failure of materials.

Another example, which compares piezoelectric transducer and optical beam deflection imaging and shows some of the depth-sensing abilities of these methods, appears in Fig. 6. The sample was an aluminum cylinder containing a 1-millimeter hole drilled subsurface at an angle of 15 degrees to the surface so that the depth of the hole varied with location on the sample. No evidence of the hole was present on the illuminated sample surface. Each line scan crossed the centerline of the buried hole at a different depth. The signal decreased approximately exponentially with hole depth for both optical beam deflection and piezoelectric transducer imaging. However, the exponential constant was approximately one thermal diffusion length for optical beam deflection imaging and two thermal diffusion lengths for piezoelectric transducer detection. These results are consistent with the analysis, which showed that optical beam deflection images are proportional to T_s, while piezoelectric transducer images sense a portion of the volume temperature field. The sample will be discussed again later in connection with electron beam and ion excitation.

ELECTRON AND ION EXCITATION

Electron and ion beams can be used as thermal imaging sources. Figure 7 is a block diagram of the instrumentation used for these studies. The electron source is a modified ETEC scanning electron microscope, where

Figure 6—Laser acoustic and laser optical beam deflection line scans of the slant hole sample.

beam blanking plates have been installed in the electron column to modulate the beam current. With this modification and a piezoelectric transducer detector attached to the specimen, it becomes a scanning electron acoustic microscope. The ion imager is a modified scanning ion mass spectrometer that also uses electrostatic beam blanking plates for modulation. In both cases, a piezoelectric transducer is used for detection.

Depth Profiling/Contrast Mechanisms in Aluminum

Figure 8 is a scanning electron acoustic microscope image of the slant hole sample described in the previous section, obtained at ≈ 70 kilohertz.[11] For reference, line scans obtained using a laser source at the same modulation frequency are also shown. Because the modulation frequency is much higher than in the prior data, the thermal diffusion length is proportionately smaller.

In the electron image, D represents the depth of the hole. Two regions are seen. Near the top of the image, $D < \delta$, and thermal contrast dominates the image, which shows the interaction of the modulated temperature with the hole. However, at the bottom of the figure, where $D >> \delta$, contrast due to the hole is still seen. The contrast cannot be thermal. Instead, it is likely that this region demonstrates the role of elastic contrast in image formation. Both ion and electron sources give virtually the same results. The similarity of the electron and laser scans suggests that for metals such as aluminum, thermoelastic signal generation processes dominate and other nonthermal beam-specimen interactions are relatively unimportant.
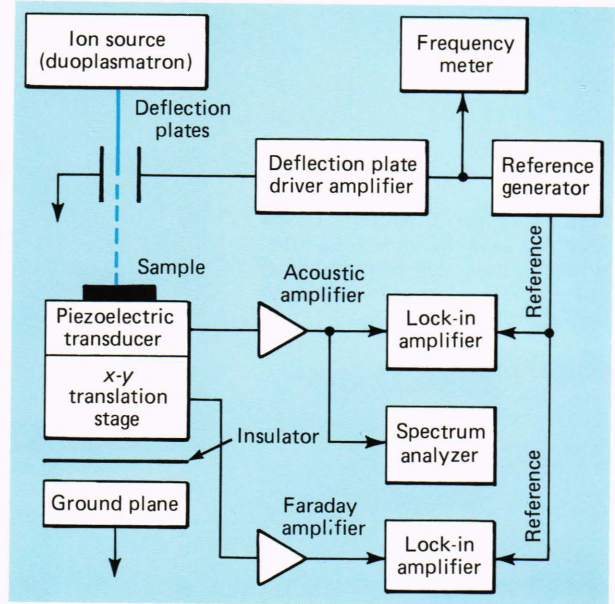

Figure 7—Block diagram of electron or ion acoustic detection system showing simultaneous detection of specimen current.

Grain Structure

Comparative scanning electron microscopy and scanning electron acoustic microscope experiments show that grain boundary structure can be observed in metals. Figure 9 shows a polycrystalline aluminum sample. The scanning electron microscope image is on the left, and the scanning electron acoustic microscope image is on the right. The contrast mechanisms are clearly differ-
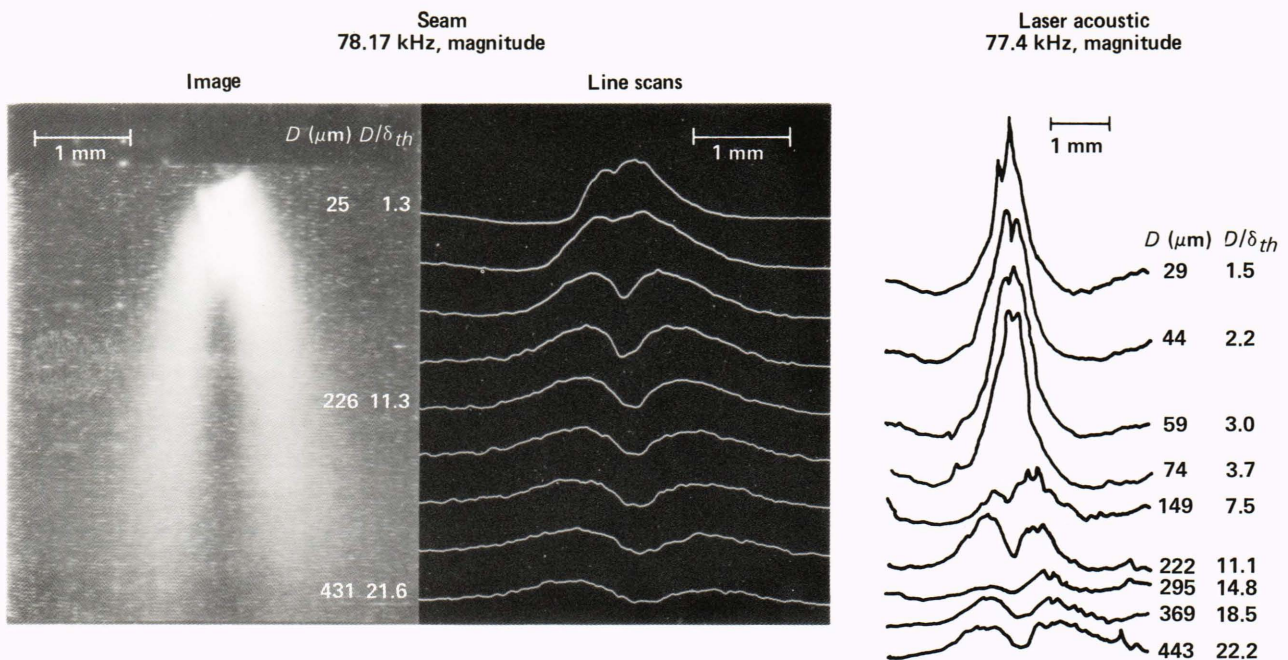

Figure 8—Electron acoustic image and line scans of slant hole sample. Laser acoustic line scans are also seen. Particle and laser excitation yields similar specimen response.

Figure 9—Electron acoustic image of grains in high-purity aluminum. Note the presence of contrast at the grain boundaries and between the interiors of grains.

Scanning electron image

Acoustic magnitude image
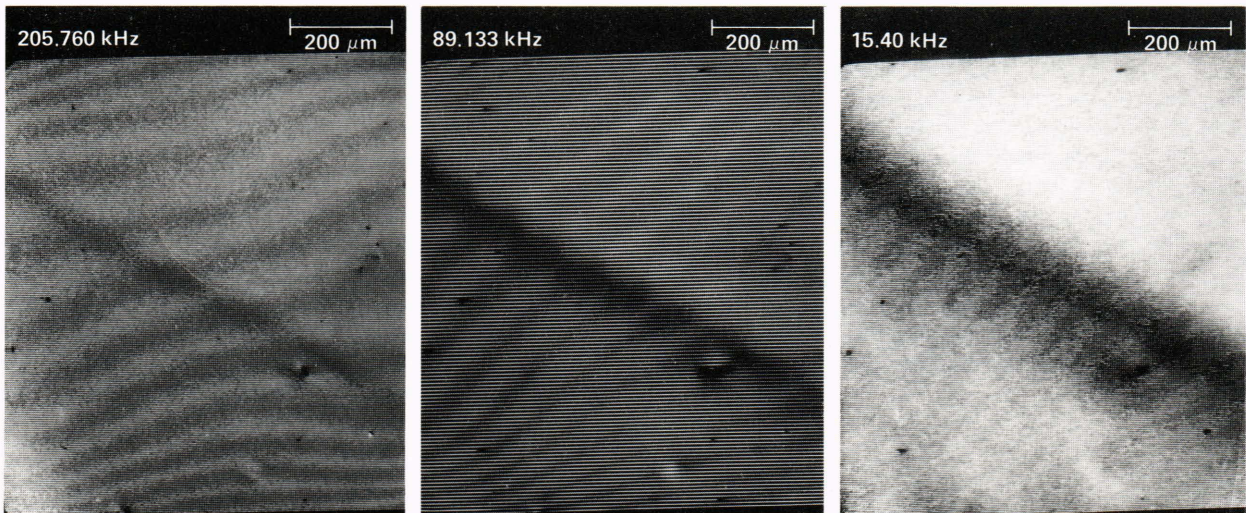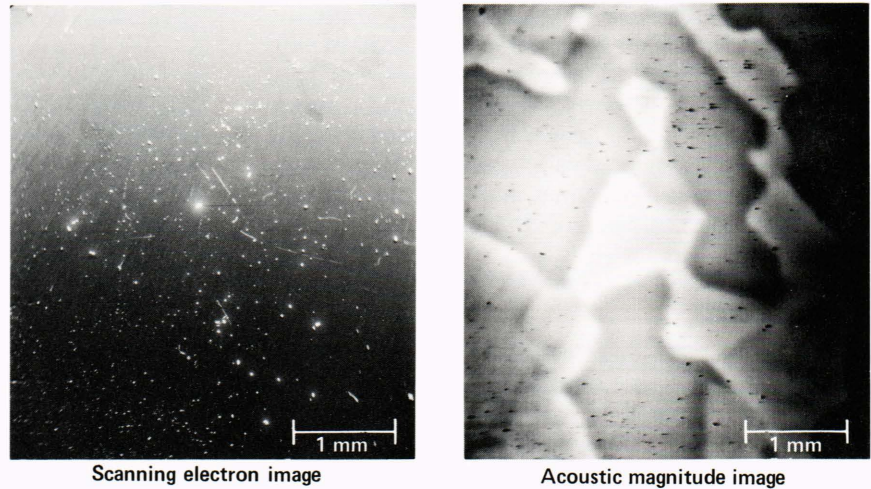
Figure 10—Grain boundary images of aluminum grains as a function of modulation frequency. The width varies as $1/\sqrt{\omega}$.

ent. Even within the scanning electron acoustic microscope image, it is possible to distinguish between contrast that occurs at the grain boundary and contrast that occurs between grains. Considering only contrast at grain boundaries, Fig. 10 shows scanning electron acoustic microscope images at various modulation frequencies, and Fig. 11 shows the dependence of the apparent boundary width on modulation frequency. This width varies as $1/\sqrt{\omega}$, a result consistent with the dependence expected for thermal contrast mechanisms where the thermal diffusion length $|\delta| = \sqrt{2\alpha/\omega}$. Figure 12 is an overlay of scanning electron acoustic microscope line scans on a scanning electron microscope image taken at fixed modulation frequency. On the right-hand side of the boundary, the amplitude of the scanning electron acoustic microscope signal varies exponentially with distance at a rate consistent with the modulation frequency. The picture relates features of the line scans of the scanning electron acoustic microscope with the grain boundary shown by the scanning electron microscope.
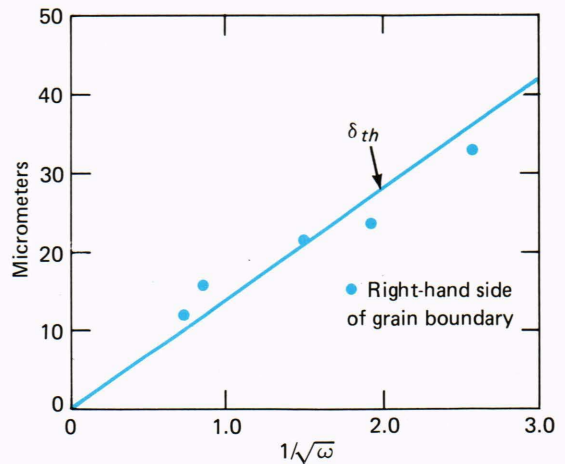
Figure 11—Plot of grain boundary width versus $1/\sqrt{\omega}$. The solid line is the thermal diffusion length of aluminum calculated using a diffusivity, α, of 1 square centimeter per second.
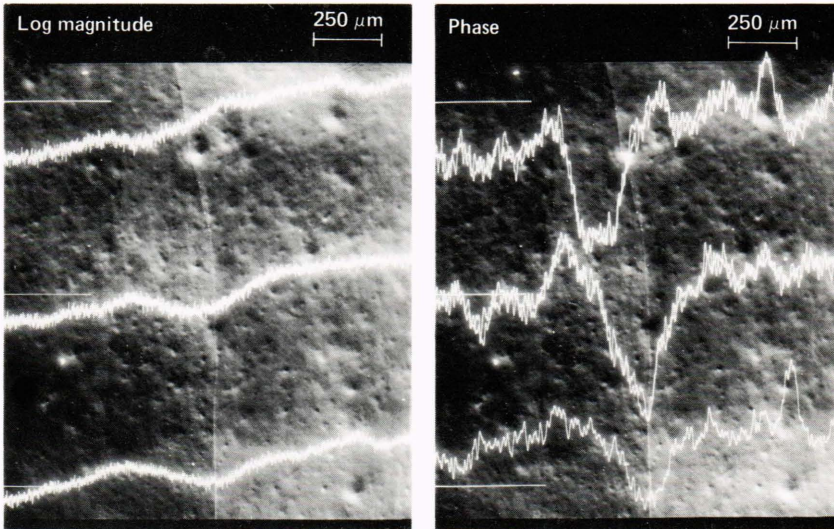
Figure 12—Scanning electron image with an overlay of electron acoustic line scans taken on a large bicrystal of aluminum. The crystal was over-etched to show the boundary. The position of the scans is indicated by the horizontal lines in the figure. Data for Fig. 12 used the response on the right-hand side of the boundary because of the interfering subsurface structure seen on the left-hand side.

The origin of the interior contrast within the grain is still an open question. In this specimen of pure aluminum, impurity segregation at the boundary and within grains should be absent. (This was confirmed with electron-induced energy-dispersive X-ray analysis of this sample. X-ray topographic studies of microstructure near the boundary were made using the Brookhaven synchrotron.) Possible sources of contrast include anisotropic elastic effects and symmetry-lowering internal stresses within grains in combination with thermally generated acoustic waves.

Particle Beam Contrast

Figures 13 and 14 suggest that the thermoelastic signal generation process is important for particle beam acoustic generation using argon ions. Figure 13 shows line scans taken using beams of argon ions at a fixed modulation frequency and various hole depths using the sample of Figs. 7 and 8. Line scans made using all three sources (ion, electron, and laser) closely resemble one another when account is taken of the different frequencies used. Figure 14 shows similar data obtained for ions at a fixed hole depth and several frequencies. Again the profiles show an approximate $1/\sqrt{\omega}$ dependence, indicating that thermal diffusion effects dominate the contrast. These experiments suggest that thermoelastic processes control acoustic signal generation for low ion beam voltages and low modulation frequencies.

BEAM-SPECIMEN CONTRAST

Interaction between the exciting beam and the specimen can give rise to image contrast and depth profiling. Figure 15 shows scanning electron microscope and scanning electron acoustic microscope images of an area of an integrated circuit at two values of primary beam voltage, V_B. For $V_B = 5$ kilovolts, the scanning electron microscope and scanning electron acoustic microscope images are essentially the same and show the surface features of the device, including areas
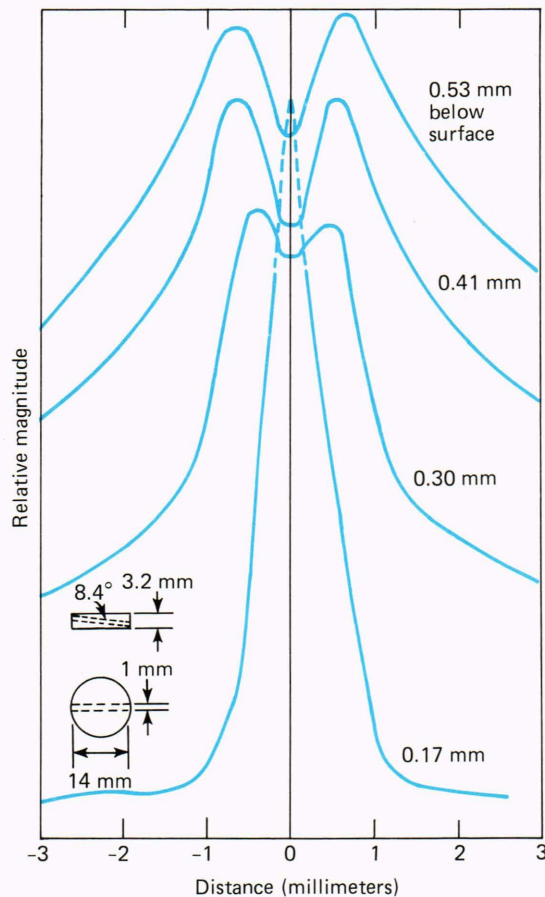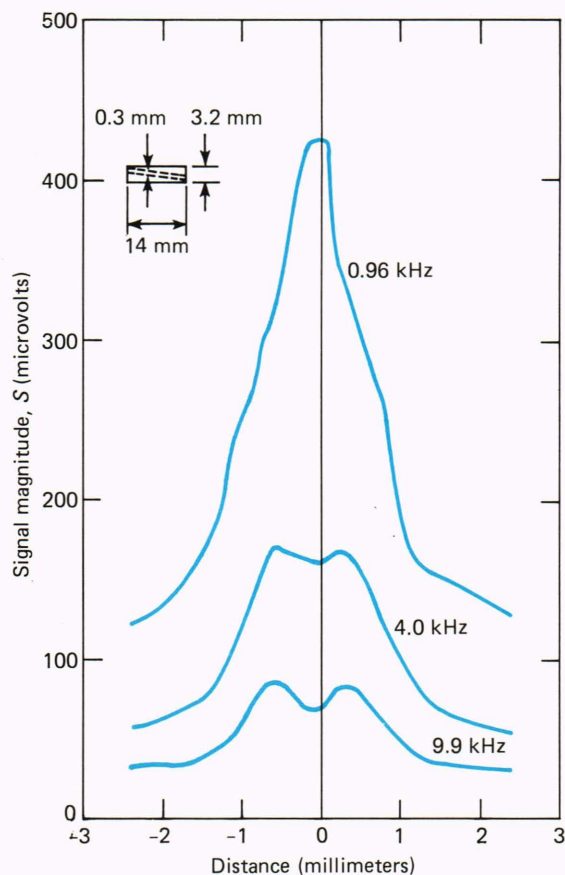

4.1 kHz; 6 keV Ar$^+$ on Al

Figure 13—Ion acoustic profiles for a slant hole sample at various depths and at 4.1 kilohertz.

of metallization. Minor differences are related to electron penetration of an ink layer covering a portion of the chip. On the other hand, the 30-kilovolt scanning electron microscope and scanning electron acoustic

Figure 14—Ion acoustic profiles for a sample containing a subsurface slant hole. At low frequencies, thermal interaction with the hole causes a signal increase. At high frequencies, the signal generation process is still thermal, but the contrast interaction is nonthermal.

microscope images are entirely different. The scanning electron acoustic microscope image shows little surface structure but strong contrast associated with a buried subsurface structure.

A second related example is shown in Fig. 16, where a scanning electron microscope image and scanning electron acoustic microscope magnitude and phase images of another integrated circuit are shown. The images presented are of the same section of the integrated circuits. Again, the scanning electron acoustic microscope images show subsurface features not visible in the scanning electron microscope image. These are thought to be related to the range of electron penetration into the sample, followed by selective interaction with different dopant regions present. Studies of the dependence of the scanning electron acoustic microscope images on V_B and ω show that at low primary voltages ($V_B \leq 5$ kilovolts) the scanning electron microscope and scanning electron acoustic microscope images are equivalent. As V_B increases, the images begin to differ, and a sequence of scanning electron acoustic microscope images becomes visible as the primary voltage is increased. These may correspond to successive layers within the chip. Some lateral resolu-

tion in the images is lost by thermal spreading. Comparison of images at 10 kilohertz with images at 400 kilohertz shows less image definition at the lower frequency. The result is consistent with an increased thermal diffusion length at the lower frequency. However, the image features remain the same, indicating that the depth profiling is not the thermal diffusion length profiling discussed previously; instead, it depends on the depth in the sample where energy is deposited. This presents a number of unresolved questions for the present understanding of the origin of the very strong contrast in Fig. 16. The role of carrier diffusion effects on the image must be clarified as well as the presence of a direct electron-lattice mechanism for stress generation. Also, the energy loss with depth in semiconductors must be re-evaluated.

Ion acoustic imaging is another area where nonthermal signal generation and image contrast processes may exist.[11] Some evidence was presented showing that the thermoelastic process is important at low frequencies. However, ion interactions with solids are known to cause a wide variety of nonthermal effects, including both sputtering and ion implantation in semiconductors and metals.[12,13] These processes are important for materials processing and for analysis. Studies of ion acoustic imaging have been conducted in order to help understand these processes better.

Sputtering is a complex process in which bombardment of a solid with energetic ions causes erosion of the surface of the solid and substantial surface and subsurface damage to the remaining material. Several mechanisms for sputtering have been suggested, including momentum transfer and thermal evaporation from regions having very high excess temperatures generated by ion-solid interactions. Most current thought favors the momentum process.

We have investigated this issue using ion acoustic imaging with the energetic rare gas ions (neon, argon, and xenon) of known primary energy to induce sputtering in several metals and nonmetals. Two types of studies were conducted. For each ion type, measurements were made of the acoustic signal as a function of primary beam voltage. Since the ratio of beam momentum to beam energy varies with voltage, the ratio of the thermoelastic signal (which is energy related) to a possible momentum transfer signal (which depends on momentum) should also vary with beam voltage.

Figure 17 shows some of the results of this study. At fixed beam voltage and variable beam current, the acoustic signal has a linear dependence on beam energy. However, at fixed current and variable voltage, the dependence deviates from linearity in the direction predicted by a momentum contribution to the acoustic signal. This result is called into question, however, by results obtained using different ions with different masses. For the same beam energy, a marked difference should exist in the acoustic signal generated by ions of different masses if the momentum transfer is an important generation process. No such difference was found, and the puzzle is still being studied.

196

5 keV, S.E. 100 μm

5 keV, φ, 480 kHz 100 μm

30 keV, S.E. 100 μm

30 keV, φ, 480 kHz 100 μm
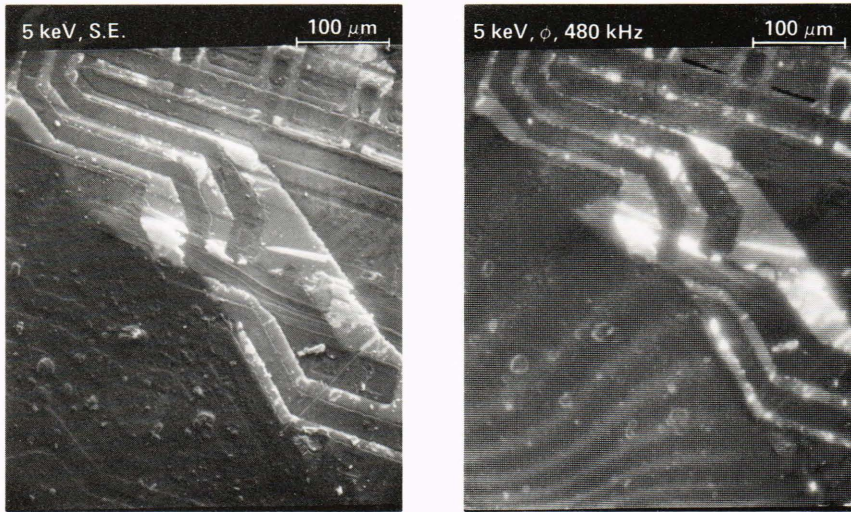
Figure 15—Scanning electron and electron acoustic images at two primary beam voltages showing beam specimen contrast.

30 kV, 42X

19 kV, 42X, 209.03 kHz, magnitude

500 μm

19kV, 42X, 209.03 kHz, phase
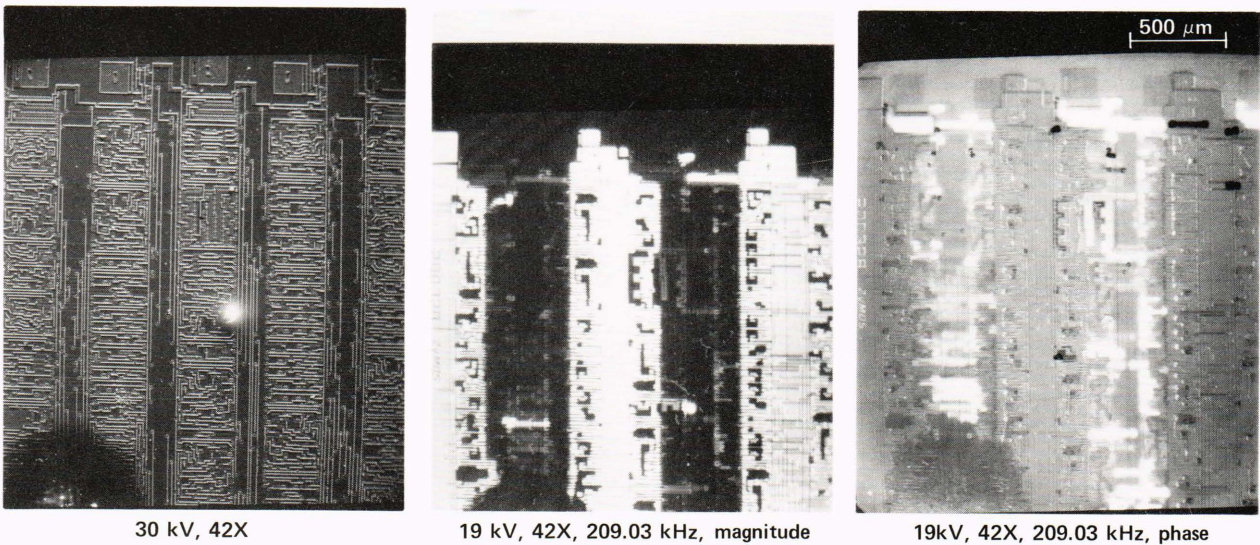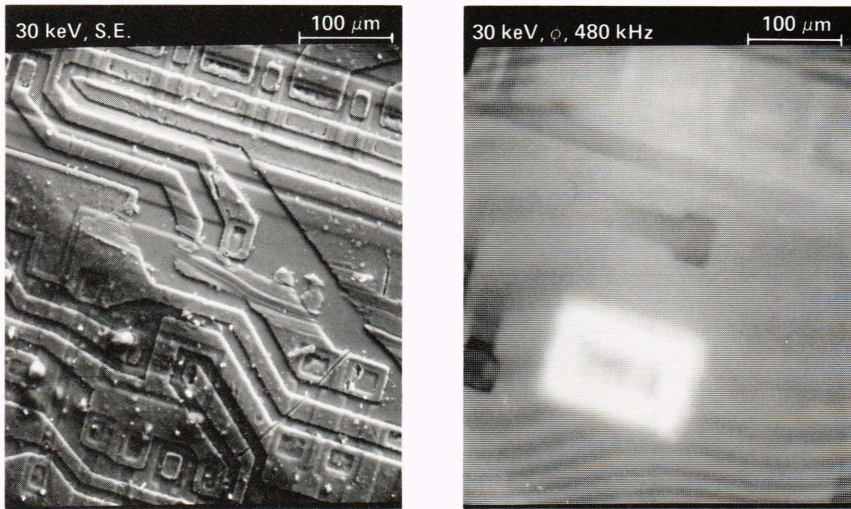
Figure 16—Scanning electron microscope and scanning electron acoustic microscope magnitude and phase images of a complementary metal oxide semiconductor chip. Subsurface structure is apparent.
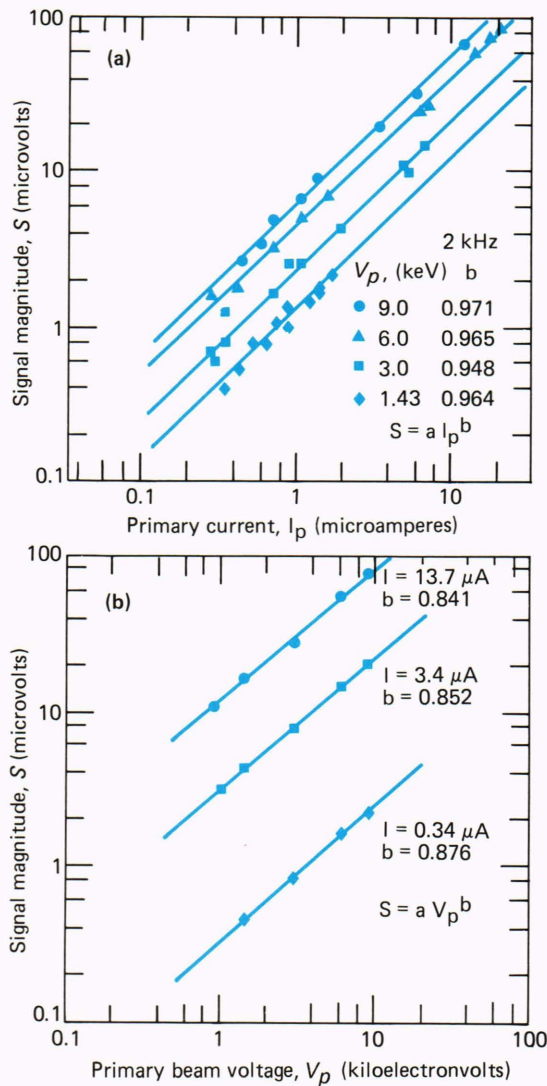
Figure 17—Dependence of ion acoustic signal on beam current (a) and on beam voltage (b).

CONCLUSION

The limited scope of this article does not reveal the broad range of physical problems that have been studied using photothermal techniques. Photothermal techniques can often be used in situ, allowing application to biological systems and other physical systems that must be measured in process. A brief list of recent work includes topics such as the curing of epoxy, properties of photosynthetic pigments, oxygen evolution in leaves and dynamics of the photosynthetic process, phase transitions, thickness of sprayed coatings, hydration of human stratum corneium (a component of skin), malarial parasites, metastable electron states of dye molecules, densification of ceramics, and fiber-matrix bonding in composites. The ability to image while making quantitative measurements of materials properties will be a significant factor in further developments in the field. However, for thermal wave imaging to become a basic and routine tool for materials analysis and processing, it is necessary to understand the basic processes involved. This begins with an understanding of beam-specimen interactions and continues through an understanding of the process of thermalization and detection.

Substantial progress has been made in this direction, but more is required to meet the minimum needs of the applications that are possible. At the present time, the imaging process and the underlying contrast mechanisms of optical beam deflection and infrared imaging methods are best understood. Some progress has been made in understanding various aspects of thermoelastic imaging using a laser source, but substantial uncertainty exists regarding the role of elastic contrast in overall image contrast. To make thermal wave imaging a quantitative tool for analyzing materials, it is necessary to resolve these issues.

REFERENCES

[1] Y. H. Wong, R. L. Thomas, and G. F. Hawkins, "Surface and Subsurface Structure of Solids by Laser Photoacoustic Spectroscopy," *Appl. Phys. Lett.* **32**, 538 (1978).
[2] W. B. Jackson, N. Amer, A. C. Boccara, and D. Fournier, "Photothermal Deflection Spectroscopy and Detection," *Appl. Opt.* **20**, 1333 (1981).
[3] J. C. Murphy and L. C. Aamodt, "Optically Detected Photothermal Imaging," *Appl. Phys. Lett.* **38**, 196 (1981).
[4] W. Nowacki, *Thermoelasticity*, Addison-Wesley, London (1962).
[5] J. C. Murphy and L. C. Aamodt, "Photoacoustic Spectroscopy of Luminescent Solids: Ruby," *J. Appl. Phys.* **49**, 3502-3509 (1977).
[6] V. A. Sablikov and V. B. Sandomirskii, "Photoacoustic Effect in Semi-Conductors," *Phys. Stat. Sol.* (B) **120**, 471-480 (1983).
[7] L. C. Aamodt and J. C. Murphy, "Effect of 3-D Heat Flow near Edges in Photothermal Measurements," *Appl. Opt.* **21**, 111 (1982).
[8] G. A. D. Briggs, "Scanning Electron Acoustic Microscopy and Scanning Acoustic Microscopy: A Favorable Comparison," *Scan. Elec. Microsc.* **III**, 1041 (1984).
[9] L. C. Aamodt and J. C. Murphy, "Photothermal Measurements Using a Localized Excitation Source," *J. Appl. Phys.* **52**, 4903 (1981).
[10] G. C. Wetsel, J. B. Spicer, J. W. Maclachlan, and J. C. Murphy, "Comparison of Photoacoustic and Photothermal Optical Beam Deflection Imaging of Subsurface Structure in Solids," in *1985 IEEE Ultrasonics Symposium Proc.*, San Francisco (Oct 1985).
[11] J. C. Murphy, J. W. Maclachlan, R. B. Givens, F. G. Satkiewicz, and L. C. Aamodt, "The Generation of Ultrasound by Laser, Electron and Ion Probes and Its Application to the Characterization of Materials," in *Proc. of Ultrasonics International 1985*, Butterworths Scientific, London (1985).
[12] O. Auciello and R. Kelly, eds., *Ion Bombardment Modification of Surfaces*, Elsevier Science Publishers, Amsterdam (1984).
[13] P. Sigmund, "Sputtering by Ion Bombardment: Theoretical Concepts," in *Topics in Applied Physics 47, Sputtering by Particle Bombardment I*, R. Behrisch, ed., Springer-Verlag, Berlin (1981).

THE AUTHORS

JOHN C. MURPHY (right) is a physicist in the Materials Science Group in the Milton S. Eisenhower Research Center. Born in Wilmington, Del., he obtained a B.A. degree from The Catholic University of America in 1957, an M.S. from Notre Dame University in 1959, and a Ph.D. from The Catholic University in 1970. His work at APL has included experimental studies of excitation transfer in luminescent systems using optical and microwave spectroscopy, measurement of nonradiative relaxation processes using photoacoustic spectroscopy, and, more recently, remote sensing of corrosion using AC magnetometry. He is currently a member of the Executive Committee of the Johns Hopkins Center for Nondestructive Evaluation, a corporately funded interdisciplinary center involving participation of the Homewood and Medical School faculties and APL's Research Center.

LEONARD C. AAMODT (seated) is a physicist in the Materials Science Group in APL's Milton S. Eisenhower Research Center. He was born in Salt Lake City and earned a B.S. degree in electrical engineering from the University of Utah in 1943 and a Ph.D. degree from Columbia University in 1955. During World War II, he worked at the Westinghouse Research Division and on the Manhattan District Project in Brooklyn, in Oak Ridge, and at Columbia University. Prior to coming to APL, he was an assistant professor in the Departments of Mathematics, Physics, and Electrical Engineering at Brigham Young University in Provo, Utah. His research interests at APL have been in the general areas of photothermal processes and thermal wave imaging.

FRANK G. SATKIEWICZ's biography and photograph can be found on p. 180.

R. BEN GIVENS (center, standing) was born in Huntington, W. Va. He graduated from the Army Electronics School in 1955 and the Capital Radio Engineering Institute in 1957. He worked as a quality control specialist for Litton Industries prior to joining APL

in 1965 and is presently an engineering staff associate in the Materials Science Group of the Milton S. Eisenhower Research Center.

P. RONALD ZARRIELLO (left) was born in Baltimore in 1933. In 1952, he joined Bendix Radio Corp., where he worked to develop the VHF electronic subsystems for jet aircraft. In 1954, he joined the JHU Radiation Laboratory in Baltimore where he worked in Dr. Jan Minkowski's group on the four-level MASER. In 1956, he joined the Los Alamos Scientific Laboratory, where he was involved in thermal shock wave testing. While working at Los Alamos, he attended the University of California and the University of New Mexico. In 1958, Mr. Zarriello returned to the JHU Radiation Laboratory and was involved in the fabrication of the first ruby laser used in experiments at Hopkins. In 1968, he joined APL's Milton S. Eisenhower Research Center, where he is now an associate engineer working in the Materials Characterization and Evaluation Group.